Open Archive TOULOUSE Archive Ouverte (OATAO)

OATAO is an open access repository that collects the work of Toulouse researchers and makes it freely available over the web where possible.

Ultrafast Nanocrystalline-TiO$_2$(B)/Carbon Nanotube Hyperdispersion Prepared via Combined Ultracentrifugation and Hydrothermal Treatments for Hybrid Supercapacitors

Katsuhiko Naoi, *Takayuki Kurita, Masayuki Abe, Takumi Furuhashi, Yuta Abe, Keita Okazaki, Junichi Miyamoto, Etsuro Iwama, Shintaro Aoyagi, Wako Naoi, and Patrice Simon*

Conventional symmetric carbon supercapacitors, also called electric double layer capacitors (EDLCs), are high power electrochemical devices with fast charging–discharging capability, remarkable stability, and cycle life.[1,2] As a result, they are used in many applications when high power is needed for a short time (few seconds). In 2012, EDLCs have entered the automobile market for stop-and-start and regeneration applications. One of the well-referred regenerative braking systems is the Mazda i-ELOOP system that can instantaneously store 25 kJ with 6 s charge during braking. However, the regenerative energy of 25 kJ, leading to –10% fuel consumption, could be increased by a factor of 3 to 5 times by designing higher-energy-density supercapacitors. A promising route to reach this goal is to design hybrid devices.[3] Recently, a new Li$_4$Ti$_5$O$_{12}$ (LTO)/ activated carbon hybrid configuration was proposed, showing ultrafast charge–discharge capability up to 300 C (=12 s), based on the use of highly dispersed single-nanocrystalline LTO (5–20 nm) grafted on multiwalled carbon nanotube (MWCNT) surface through in situ ultracentrifugation (UC) process.[3,4] Other materials such as Nb$_2$O$_5$, V$_2$O$_5$, H$_2$Ti$_3$O$_7$, and TiO$_2$ have been reported as a negative electrode for hybrid capacitors.[5–9]

Prof. K. Naoi, T. Kurita, M. Abe, T. Furuhashi, Y. Abe,
K. Okazaki, Dr. J. Miyamoto, Dr. E. Iwama, S. Aoyagi
Department of Applied Chemistry
Tokyo University of Agriculture & Technology
2-24-16 Naka-cho, Koganei, Tokyo 184-8558, Japan
E-mail: k-naoi@cc.tuat.ac.jp
Prof. K. Naoi, W. Naoi
Division of Art and Innovative Technologies
K & W Inc.
1-3-16-901 Higashi, Kunitachi, Tokyo 186-0002, Japan
Prof. K. Naoi, Dr. J. Miyamoto
Advanced Capacitor Research Center
Tokyo University of Agriculture & Technology
2-24-16 Naka-cho, Koganei, Tokyo 184-8558, Japan
Prof. K. Naoi, Dr. J. Miyamoto, Dr. E. Iwama, Prof. P. Simon
Global Innovation Research Organization
Tokyo University of Agriculture & Technology
2-24-16 Naka-cho, Koganei, Tokyo 184-8558, Japan
Prof. P. Simon
CIRIMAT, Université de Toulouse, CNRS, INPT, UPS
118 route de Narbonne, Toulouse 31062, Cedex 9, France
Prof. P. Simon
Réseau sur le Stockage Electrochimique de l'Energie (RS2E)
FR CNRS
3459, France

V$_2$O$_5$ nanotubes show relatively high rate-capability (up to 30 C) within a voltage range between 1.6 and 4.0 V versus Li/Li$^+$.[7] Nb$_2$O$_5$ (T-Nb$_2$O$_5$) nanoparticles can maintain 67% of its theoretical capacity at high rate (60 C) within a voltage range between 1.2 and 3.0 V versus Li/Li$^+$.[8] H$_2$Ti$_3$O$_7$ nanowires exhibit fast psuedocapacitive behavior (up to 20 C) when charged and discharged down to 1.0 V versus Li/Li$^+$.[9] However, despite important advances, these materials fail to reach very high charge/ discharge rates needed for hybrid supercapacitor applications (>100 C). In the present article, we focus on bronze-type TiO$_2$ (TiO$_2$(B)) which has a much higher electric conductivity ($\approx$10^{-2} S cm^{-1}) compared to other TiO$_2$ polymorphs such as anatase and rutile (10^{-14}–10^{-13} S cm^{-1}).[10] TiO$_2$(B) shows a theoretical capacity of 335 mAh g^{-1} during Li$^+$ ion intercalation, where Li$^+$ diffusion proceeds along the b-axis tunnel giving poor Li$^+$ diffusion coefficient of 10^{-14}–10^{-16} cm^2 s^{-1}.[11] Conventional TiO$_2$(B) synthesis, via hydrothermal treatment from alkaline titanates giving cylindrical morphology with long b-axis, results in poor C-rate capability up to 6 C.[12–14] TiO$_2$(B)/MWCNT or graphene composites exhibit decent capacity (110–200 mAh g^{-1}) thanks to the conducting MWCNT or graphene, yet their operated C-rate is limited in a 4.5–18 C range.[15–17] Downsizing the particle size (3–10 nm) enabled a C-rate operation up to 60 C with more than 50% capacity retention obtained at low C-rate.[18–21] Operation over 100 C, however, has been hampered because of the inevitable agglomeration of TiO$_2$(B) nanoparticles,[18–21] that limits the accessibility of Li$^+$ from the bulk electrolyte. Nano-TiO$_2$(B)/carbon composites using activated carbon fiber or reduced graphene oxide have less TiO$_2$(B) reagglomeration, but often produce the undesirable growth of TiO$_2$(B) in b-axis dimension.[22–24] Introducing nitrogen atoms either on TiO$_2$(B) (N-doped TiO$_2$(B))[25] or the composite carbon (N-doped graphene)[26] further improved the rate-capability of TiO$_2$(B), yet failed to maintain the 50% capacity retention over 100 C.

Here, we report about the synthesis of nanosized TiO$_2$(B)/ MWCNT composites, called uc-TiO$_2$(B)/MWCNT. The uniformly hyper-dispersed single-nano TiO$_2$(B) crystals were formed within MWCNT matrix, via UC treatment combined with a follow-up hydrothermal treatment. The uc-TiO$_2$(B)/ MWCNT has size-controlled crystalline TiO$_2$(B) particles (5 nm in average) and anisotropic crystal growth (ultrashort along b-axis) restricting the TiO$_2$(B) nanoparticles from agglomerating. These features improve the power capability of TiO$_2$(B) by enabling ultrafast Li$^+$ deintercalation (235 mAh g^{-1} at 300 C, 1 C = 335 mA g^{-1}), paving the way for designing the next generation of high power and high energy hybrid supercapacitors.

The dispersion of TiO₂(B) nanoparticles within the carbon matrix is one of the key features for achieving high rate capability. Distinct from previous studies,[12–14,18–26] the ultracentrifugation process (UC treatment) with follow-up hydrothermal treatment allows the formation of single-nanosized and hyper-dispersed TiO₂(B) on the surface of MWCNTs. First, the successful TiO₂(B) formation was confirmed by the XRD pattern (Figure S1, Supporting Information), where only small peaks of TiO₂ rutile due to the agglomeration of rutile particles can be seen (Figure S2, Supporting Information). The four main peaks for the (001), (110), (002), and (003) planes can be observed, in good agreement with the reference of TiO₂(B) crystals and TiO₂(B) prepared from the tetranuclear complex [Ti₄(C₂H₂O₃)₄(C₂H₃O₃)₂(O₂)₄O₂(H₃O)₆].[27] The crystallite sizes were calculated using the Scherrer formula. The calculated diameters of the TiO₂(B) crystallites are 3–6 nm for the TiO₂(B)/MWCNT (70/30) composite. These crystallite sizes are in good agreement with those reported for TiO₂(B) crystalline synthesized from tetranuclear Ti complex via hydrothermal method.[21,22] **Figure 1**a shows that nanosized TiO₂(B) particles have been homogeneously dispersed into the MWCNT matrix. This unique structure was obtained thanks to UC treatment, which disentangles MWCNT matrix during ultracentrifugation of 75 000 g. The highly dispersed
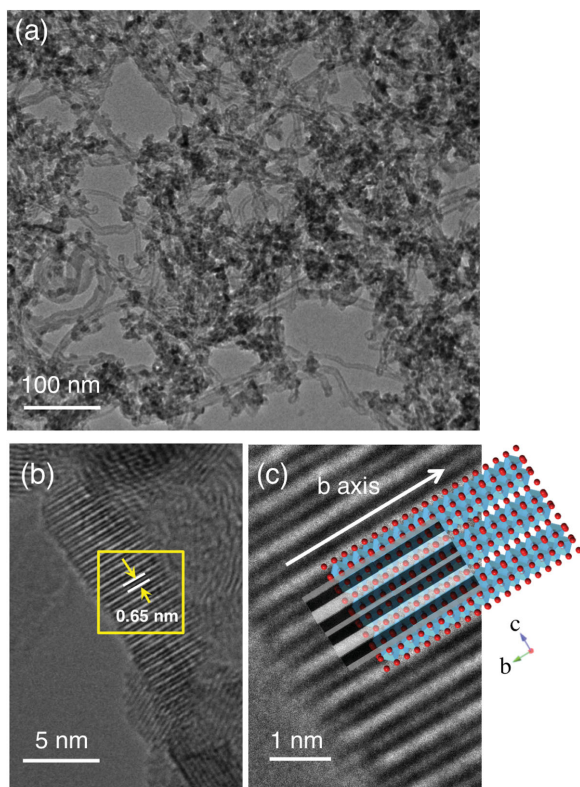

Figure 1. HRTEM images for ultracentrifugation (uc)-TiO₂(B)/MWCNT (70/30) composite. a) Lower magnification (30 000×) image for a highly dispersed uniform-sized TiO₂(B) nanocrystals within MWCNT matrix. b) Focus on a representative TiO₂(B) single nanoparticle, showing clear lattice fringes of d = 0.65 nm corresponding to the (001) plane. c) Magnified view of the image (b) with a complete match of (001) plane pattern of the model TiO₂(B) lattice, indicative of anisotropic characteristics of the crystal which is ultrashort along b-axis.

[Ti₄(C₂H₂O₃)₄(C₂H₃O₃)₂(O₂)₄O₂(H₃O)₆] is absorbed on the exposed MWCNT surface, so that the agglomeration of nanoparticles can be avoided during the transformation of Ti complex into TiO₂(B) under the subsequent hydrothermal treatment. High-resolution transmission electron microscopy (HRTEM) image (Figure S3, Supporting Information) shows lattice fringes and facets in all the TiO₂(B) nanoparticles, while the sides and planes of each particles are well-attached onto the outer surface of MWCNT. Among the observed TiO₂(B) nanoparticles, typical lattice patterns can be seen as shown in Figure 1b; most of the pattern can be assigned to the (001) plane with 0.65 nm lattice spacing. To determine the axis direction of the TiO₂(B) crystal with such (001) planes in the HRTEM image, we overlapped the image of TiO₂(B) crystal unit (obtained from CrystalMaker ver. 9, HULINKS) with the TEM image (Figure 1c). Interestingly, the shortest side of TiO₂(B) crystal (3–5 nm) corresponds to the b-axis of the image, suggesting successful control of TiO₂(B) growth along the b-axis. Figure S4 of the Supporting Information shows the thermogravimetric plots of the TiO₂(B)/MWCNT composites. The MWCNT ratio was 31 wt% for the typical sample with TiO₂(B)/MWCNT (70/30), indicating that the nano-TiO₂(B) crystallization proceeded without any undesirable side reaction such as carbon consumption via oxidation. The loading amount of TiO₂(B) appears to strongly depend on the effective specific surface area of the nanocarbon matrix (270 m² g⁻¹ for the MWCNT). We also attempted to synthesize TiO₂(B)/MWCNT composites (80/20), which are suitable for increasing the total energy density of the composite. The obtained stoichiometry of TiO₂(B)/MWCNT (67/33) means that 12–13 wt% of TiO₂(B) were lost during the synthesis. Such a loss of TiO₂(B) indicates the existence of unanchored TiO₂(B) on the MWCNT matrix, which must have been extracted during filtration, suggesting a limitation from the available MWCNT surface area (20 wt%) to anchor all of TiO₂(B) nanoparticles (80 wt%). In this study, we selected the TiO₂(B)/MWCNT (70/30) composition to balance the performance in terms of energy density and rate capability.

The electrochemical responses of ultrashort b-axis TiO₂(B) nanoparticles were characterized by charge–discharge tests. Typical charge (deintercalation)–discharge (intercalation) curves[21] for TiO₂(B)/MWCNT (70/30) tested at 1 C-rate (1 C = 335 mA g⁻¹) are shown in **Figure 2**a. The TiO₂(B)/MWCNT electrode has sloping plateau around 1.6 V versus Li/Li⁺ with a capacity of 275 mAh g⁻¹ per TiO₂(B), corresponding to the 82% of the theoretical capacity. Such a high utilization of TiO₂(B) was owing to the successful synthesis of 5 nm average TiO₂(B) nanoparticles with ultrashort 3–5 nm b-axis length firmly attached on the MWCNT surface, without agglomeration. In the cyclic voltammogram at 56 μV s⁻¹ (Figure 2b), sharp twin peaks can be easily observed at 1.65 and 1.55 V versus Li/Li⁺, which are related to A1 and A2 intercalation sites, respectively.[28–31] The absence of any peaks at 1.8–2.0 V versusLi/Li⁺ confirms that no TiO₂ anatase was present in the sample. A cavity microelectrode was used to evaluate the kinetic impact of the short b-axis in TiO₂(B) crystal. The total measured current of the obtained cyclic voltammograms (Figure S5, Supporting Information) can be divided into two contributions by the equation

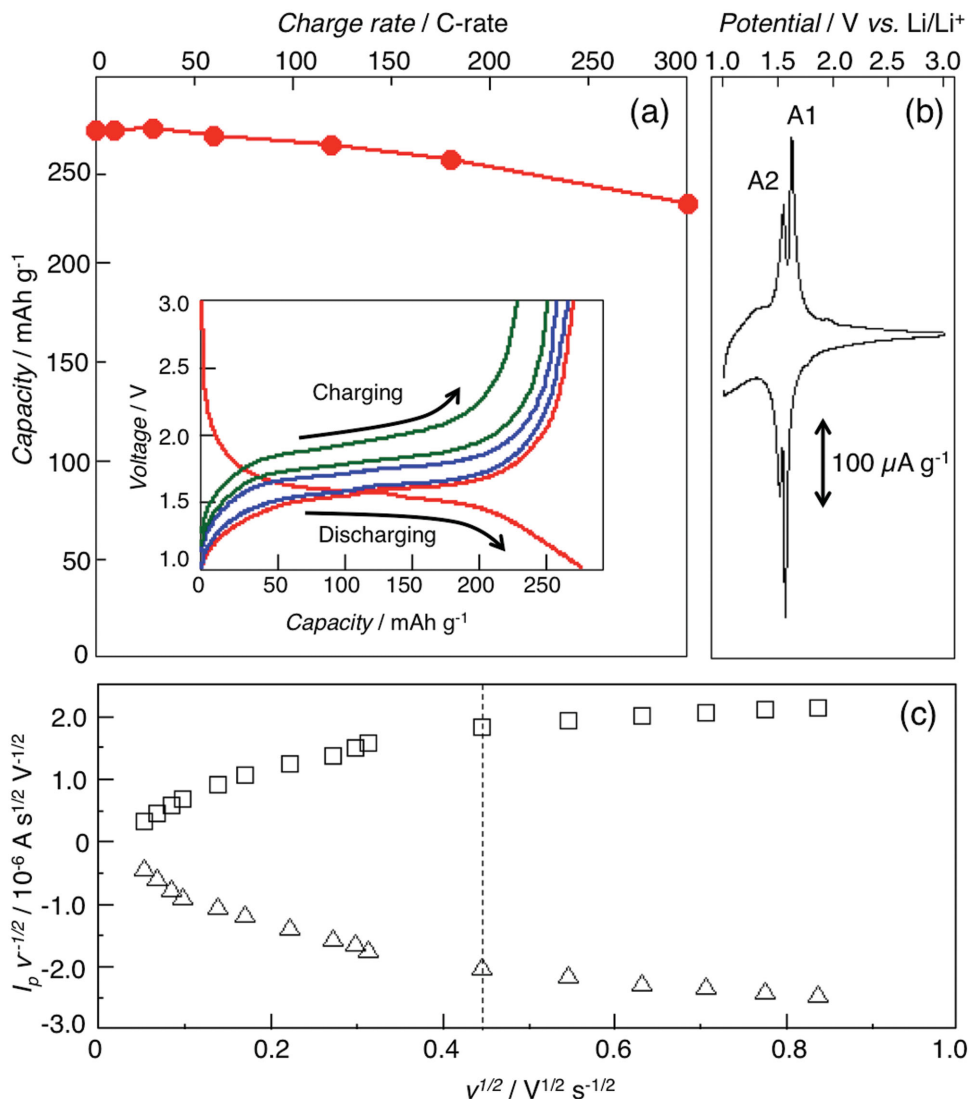$$I_p/v^{1/2} = k_1 v^{1/2} + k_2 \qquad (1)$$

Figure 2. a) Plots of charge capacity per TiO$_2$(B) as a function of C-rate with fixed discharge C-rate, assuming as 1 C = 335 mA g^{-1}. Inset: Potential profiles at five different charge C-rates of 1, 60, 120, 180, and 300 C, along with the discharge curve at 1 C. b) Cyclic voltammogram (CV) at the scan rate of 56 μV s^{-1}. c) Plots of $I_p \, v^{-1/2}$ versus $v^{1/2}$ obtained at 18 different scan rates ranged from 0.001 to 0.7 V s^{-1} using a cavity microelectrode.

where I_p, and v stand for the peak intensity in A and the scan rate in V s^{-1}, respectively. k_1 coefficient is associated with a fast, nondiffusion-limited surface process, while k_2 defines diffusion-limited faradic reaction.[32] Assuming that the current for TiO$_2$(B) is rate-determined by Li$^+$ diffusion along the b-axis, we plotted the $I_p \, v^{-1/2}$ using A1 peak current against $v^{1/2}$. Figure 2c shows the $I_p \, v^{-1/2}$ versus $v^{1/2}$ plots from 0.001 to 0.7 V s^{-1} for the TiO$_2$(B)/MWCNT (70/30). The plots can be divided into two regions (dotted line in Figure 2c): a sloping region at the scan rates below 300 mV s^{-1}, and a nearly flat region. The sloping region shows high k_1 contribution (more than 90%) to the total of $k_1 + k_2$, which evidences a non-Li$^+$ diffusion limited reaction of TiO$_2$(B) at slow scan rate. The maximum scan rate of the slope region, 300 mV s^{-1} is a much higher value compared to the other reported value (LiFePO$_4$, 140 nm in average),[32] which is limited up to 5 mV s^{-1}. Interestingly, even the nearly flat region has a k_1 contribution of 40%, unlike the reported

LiFePO$_4$ whose k_1 contribution over 5 mV s^{-1} is close to 0. The results of cavity microelectrode demonstrates the ultrafast Li$^+$ kinetics in the uc-TiO$_2$(B) with ultrashort b-axis. The contribution of nondiffusion-limited (NDL) surface process to the total current has been calculated/compared at two different scan rates of 1 mV s^{-1} (Figure S6a, Supporting Information) and 100 mV s^{-1} (Figure S6b, Supporting Information). Such analysis was made following the procedure already reported in references.[6,33] The calculated contributions denoted both in red at low (1 mV s^{-1}) and high (100 mV s^{-1}) scan rates did not show any appreciable difference from the respective total currents at the same scan rates. This means that the NDL surface process is the dominating process in the time frame investigated. This clearly indicates an exceptionally ultrafast performance of uc-TiO$_2$(B) due mainly to the shortened b-axis diffusion length. Such feature is unique and not observed in other previous works.[6,33]

The pore size distribution of the matrix is also a critical factor for fast electrochemical response. Figure S7 of the Supporting Information shows the pore size distribution of the composites obtained from N_2 absorption isotherm using BJH model. The main broad peak from 10 to 100 nm is attributed to the pores of the pristine MWCNT entanglements on the BJH curve shape, while the interparticle pore in $TiO_2(B)$ agglomeration (see Figure S8a–c, Supporting Information) from 3.4 to 7 nm appears separately from the MWCNT pore distribution. The results indicate the contribution from the remaining MWCNT pore within the composites, which can act as a reservoir of Li^+-containing electrolyte and supply sufficient Li^+ to the surface of $TiO_2(B)$ nanoparticles at high-rate charge–discharge operation. The electrochemical performance depends on the way the TiO_2 nanoparticles are agglomerated or dispersed onto the MWCNT surface. The ratio of the $TiO_2(B)$ agglomeration ($R_{agglom.TiO_2(B)}$) was evaluated from the equation

$$R_{agglom.TiO_2(B)} = V_{agglom.}/V_{agglom.\ pure\ TiO_2\ (B)} = 3.469 * V_{agglom.}\ [-] \qquad (2)$$

where V_{agglom} and $V_{agglom.\ pure\ TiO2(B)}$ stand for the volume of the interparticle pore in the composite $TiO_2(B)$ agglomeration and the volume of the interparticle pore in the pure $TiO_2(B)$ agglomeration, respectively (see Figure S8d,e, Supporting Information). V_{agglom} can be calculated by integrating dV $d\log(D)^{-1}$ profile for the objective $TiO_2(B)$/MWCNT composites in Figure S7 of the Supporting Information between 3.4 and 7 nm, and subtracting the contribution from the MWCNT background. The value of $V_{agglom.\ pure\ TiO2(B)}$ (= 0.3059 $cm^3\ g^{-1}$) was obtained with same calculation, but for the pure $TiO_2(B)$ agglomeration whose BJH profile can be seen in Figure S7a of the Supporting Information. Then, the dispersibility of $TiO_2(B)$ ($D_{TiO2(B)}$) was calculated from the equation

$$D_{TiO_2(B)} = 1 - R_{agglom.TiO_2(B)} = 1 - 3.469 * V_{agglom}\ [-] \qquad (3)$$

Figure 3 shows specific discharge capacity plots of $TiO_2(B)$ at 1 and 300 C versus calculated $D_{TiO2(B)}$. The linear correlation between the capacity and $D_{TiO2(B)}$ shows the capacity of $TiO_2(B)$ is strongly dependent on the dispersion factor of $TiO_2(B)$ within $TiO_2(B)$/MWCNT composites. The extrapolated capacity at $D_{TiO2(B)}$ = 100, corresponding to the $TiO_2(B)$ nanoparticles (5 nm size) without any agglomeration, reaches the theoretical value of $TiO_2(B)$ (335 mAh g^{-1}). Cyclic voltammograms for $TiO_2(B)$/MWCNT composites are shown with different $D_{TiO2(B)}$ (= (a) 0.35, (b) 0.65, and (c) 0.87, with the corresponding TEM images, see Figure S9, Supporting Information) at different scan rates ranging from 56 to 2780 μV s^{-1} (Figure 3 inset). The overall shape of CV at slow scan rates (<278 μV s^{-1}) is more or less similar, having two redox peaks at 1.55 and 1.65 V versus Li/Li^+. At higher scan rates (>556 μV s^{-1}), however, the CV shapes for low-$D_{TiO2(B)}$ composites (a) become distorted with large peak voltage difference (ΔV_p) shifts, while those for middle and high-$D_{TiO2(B)}$ composites (b) and (c) maintain their shapes with smaller ΔV_p shifts, showing the $D_{TiO2(B)}$ influence on the high rate capability.

b-axis length of $TiO_2(B)$ is another important factor for high rate-capability. For comparison purposes, we prepared rod-type $TiO_2(B)$ crystals with long b-axis (L-$TiO_2(B)$), that contains
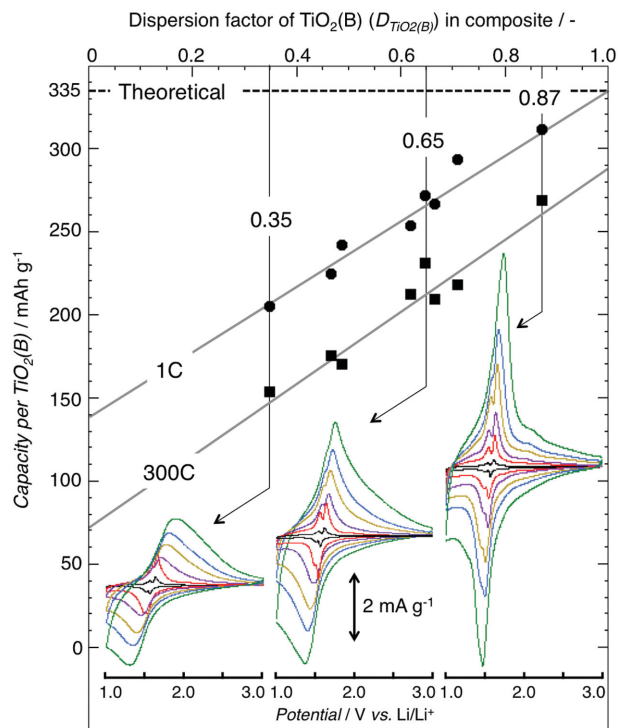

Figure 3. Charge capacity per $TiO_2(B)$ as a function of the dispersion factor ($D_{TiO_2(B)}$) of $TiO_2(B)$ in the composite. The capacity was obtained at two different charging rates of 1 and 300 C and show linear relationship against the dispersion factor. Inset: Cyclic voltammogram (CV)s of three typical $D_{TiO2(B)}$ of 0.35, 0.65, and 0.87. The CVs are obtained at six different scan rates ranged from 56, 278, 556, 1110, 1680 to 2760 μV s^{-1}.

same amount of MWCNT (30 wt%) as the short b-axis $TiO_2(B)$ (S-$TiO_2(B)$). The TEM image of L-$TiO_2(B)$ in Figure S10 of the Supporting Information shows that the 40–60 nm long $TiO_2(B)$ nanorods are dispersed within the MWCNT matrix. The TEM image comparison between S- and L-$TiO_2(B)$ highlights significant difference in the b-axis length and path number (**Figure 4**a); one typical S-$TiO_2(B)$ nanoparticle has eight times shorter b-axis in length and four times larger number of diffusion channels compared to L-$TiO_2(B)$. The sharpened b-axis peak (020) compared to the other as (003) and (60-1) peaks for the L-$TiO_2(B)$ confirms the length of b-axis in the $TiO_2(B)$ (Figure 4a inset). Cyclic voltammograms for S-and L-$TiO_2(B)$ at 10 mV s^{-1} (Figure S11, Supporting Information) shows that the shape and the number of the peaks are different between the two samples; the S-$TiO_2(B)$ shows two sharp peaks at 1.55 and 1.65 V versus Li/Li^+, while the L-$TiO_2(B)$ possesses one broaden peak which is similar to the reported CV shape of $TiO_2(B)$ nanowire with 20–40 nm of diameter and 1–5 μm length.[34] The sharpening of the peaks for S-$TiO_2(B)$ comes from the shortening of b-axis length and the increased number of diffusion paths, which enable a fast Li^+ access and intercalation into $TiO_2(B)$ A1 and A2 sites along the b-axis diffusion channel in the $TiO_2(B)$ crystals (Figure S11a, Supporting Information), while the L-$TiO_2(B)$ shows random Li^+ intercalation into A1 and A2 sites due to the energy dissipation along the long b-axis diffusion paths (Figure S11b, Supporting Information). Charge–discharge curves for L-$TiO_2(B)$/MWCNT (70/30) are
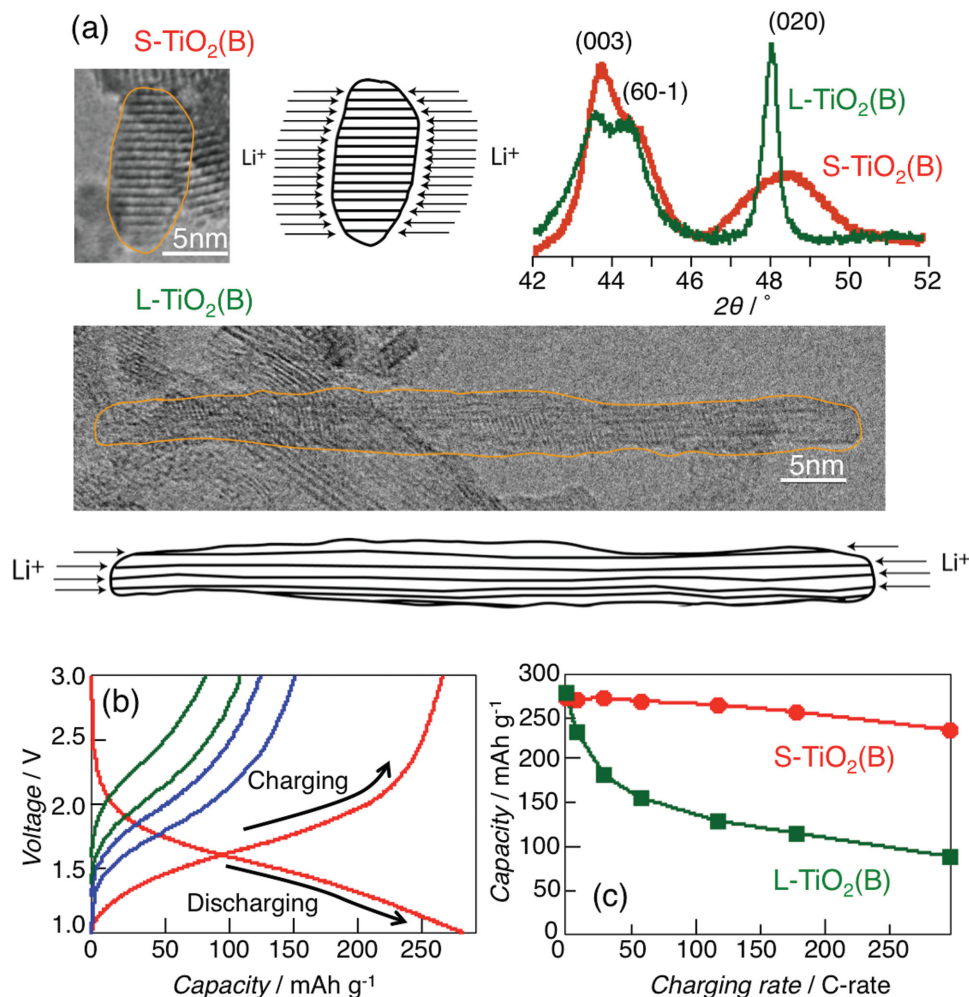
Figure 4. a) Representative HRTEM images and their schematic illustrations for short *b*-axis TiO$_2$(B) (S-TiO$_2$(B), *b*-axis length = 3–5 nm)) and long *b*-axis TiO$_2$(B) (L-TiO$_2$(B), *b*-axis length = 40–60 nm) nanocrystals showing significant difference in number/depth of diffusion pathways for two crystals. Inset: XRD patterns for S-TiO$_2$(B) (red) and L-TiO$_2$(B) (green) shown in the narrow bands of $2\theta = 42°–52°$, featuring the distinct difference in the I(020)/(I(003) or I(60-1)) which corresponds to *b*-axis/(*a*-axis or *c*-axis) namely the aspect ratio of the crystals. b) Potential profiles for L-TiO$_2$(B) at five different discharge C-rates of 1, 60, 120, 180, and 300 C, along with the charge curve at 1 C. c) C-rate dependency of the charge capacity per TiO$_2$(B) for S-TiO$_2$(B) (red) and L-TiO$_2$(B) (green).

shown in Figure 4b. At 1 C in charge, the L-TiO$_2$(B)/MWCNT electrode has sloping plateau around at 1.6 V versus Li/Li$^+$ with the capacity of 280 mAh g^{-1} per TiO$_2$(B), corresponding to the 84% of its theoretical capacity. This high utilization of TiO$_2$(B) is more or less the same value as that of S-TiO$_2$(B)/MWCNT, showing that the synthesis of highly dispersed L-TiO$_2$(B)/MWCNT was successful. At the higher scan rates over 30 C, however, the curve slope became steeper and the exhibited charge capacity became smaller, unlike S-TiO$_2$(B) which showed ultrafast rate-capability. The summarized results of charge rate capability tests for S- and L-TiO$_2$(B) in Figure 4c clearly show the clear superiority of ultrashort *b*-axis (3–5 nm, S-TiO$_2$(B)) to the long one (40–60 nm, L-TiO$_2$(B)).

In summary, nanoscale (average length = 5 nm in *b*-axis) bronze-type TiO$_2$ (TiO$_2$(B)) particles were prepared onto MWCNT by an UC process, followed-up by hydrothermal (HT) treatment. Four-nuclear complexes, hyper-dispersed within a MWCNT matrix in aqueous media precursors by UC treatment,

were subjected to the follow-up HT treatment to prepare highly crystalline nanosized (5nm in average) TiO$_2$(B)/MWCNT composites (uc-TiO$_2$(B)/MWCNT). The uc-TiO$_2$(B)/MWCNT composite shows a hyperdispersion of nanocrystalline TiO$_2$(B) within the MWCNT matrix, with a minimized growth in the direction of *b*-axis length (3–5 nm). The uc-TiO$_2$(B)/MWCNT composite electrodes were electrochemically characterized by charge–discharge cycling tests at various C-rates, from 1 to 300 C. The electrode showed excellent power capability with 275 mAh g^{-1} delivered at 1 C and 235 mAh g^{-1} at 300 C. This is a solid demonstration of the ultrafast behavior of the uc-TiO$_2$(B)/MWCNT composite that can be used to prepare hybrid supercapacitors with higher energy density.

Experimental Section

Materials: Hydrogen peroxide solution (30%), ammonia water (28%), glycolic acid (>97%), and sulfuric acid (>97%) (Wako Pure Chemical

Industries) as well as Ti metal (>99.99%, Sigma-Aldrich) were used to prepare the composites. MWCNT with specific surface area of 270 m^2 g^{-1} was provided by Mitsubishi Materials Corporation.

Preparation of uc-TiO$_2$(B)/MWCNT Composites: UC process is an in situ build-up synthesis, yielding to nano composites obtained by hyperagitation of ultracentrifugation under 75 000 g (corresponding to 20 000 rpm). The UC process is different from any other conventional separation (purification) methods. The details of the UC treatment have been described elsewhere.[3,4,35,36] UC treatment is not effective to unbundle the MWCNTs but drives a disentanglement/dispersion of the MWCNTs;[4,36] aside, there is practically no appreciable change in BET surface area (240 ± 30 m^2 g^{-1}) with or without the UC treatment. The main synthesis procedures of the uc-TiO$_2$(B)/MWCNT involve the following three steps 1, 2, and 3:

(1) Prior to UC treatment, water-soluble four-nuclear titanium complex [$Ti_4(C_2H_2O_3)_4(C_2H_3O_3)_2(O_2)_4O_2(H_3O)_6$][27] was prepared as an appropriate precursor for generating pure-phase TiO$_2$(B).
(2) The precursor was then subjected to the UC treatment that leads to uniform dispersion/disentanglement as well as effective adsorption of the [$Ti_4(C_2H_2O_3)_4(C_2H_3O_3)_2(O_2)_4O_2(H_3O)_6$] complex onto the exposed surface of MWCNT under ultracentrifugation.
(3) Finally, the dispersion was hydrothermally treated, which allows the crystallization of the single-nano TiO$_2$(B) under careful control of pH, temperature, and operational duration to prevent major impurity phases such as TiO$_2$ anatase.

These permit the synthesis of single-nano (≈5 nm) TiO$_2$(B), highly dispersed and absorbed on the MWCNT surface, with minimized impurity phases of TiO$_2$ rutile; no TiO$_2$ anatase and other polymorphs were observed.

First, 0.180 g of Ti metal was dissolved into 13.30 mL of hydrogen peroxide solution and 4.20 mL of ammonia water. After the addition of 0.428 g of glycolic acid in the solution under stirring, the solution was heated at 80 °C for 3 h in a water bath to form dried yellow-colored water-soluble Ti complex; [$Ti_4(C_2H_2O_3)_4(C_2H_3O_3)_2(O_2)_4O_2(H_3O)_6$] (corresponding to the step 1 described above). The obtained yellow powder was dissolved in 25.0 mL of distilled water and filtered. After addition of an excess of the glycolic acid (0.857 g) and MWCNT (0.129 g), the dispersion was subjected to UC treatment under mechanochemical agitation **(step 2)**. The pH of the solution was controlled to 1 by addition of sulfuric acid. Then, this mixture was heated in a Teflon autoclave at 200 °C for 2 h to form a TiO$_2$(B)/MWCNT composite **(step 3)**. The TiO$_2$(B)/MWCNT composite was then separated from the solution by centrifugation, and the powder was dried at 80 °C for 17 h. Finally, purification of the TiO$_2$(B)/MWCNT composites was made by removing the residual organic compounds at 300 °C for 5h to be TiO$_2$(B)/MWCNT (70:30 in wt%) in the final product.

Physicochemical Characterization of the uc-TiO$_2$(B)/MWCNT: TiO$_2$(B)/MWCNT nanostructure and particle size distribution were characterized using HRTEM (Japan, Hitachi model H9500, 300 kV), and the crystal structure was analyzed using X-ray diffraction (XRD, Rigaku SmartLab, Cu Kα radiation λ = 1.54056, operating at 45 kV–200 mA). The XRD patterns were recorded between 10° and 60° with a step rate of 0.1° min^{-1}. Thermogravimetric analysis (TGA) was performed under synthetic air using a thermogravimetric and differential thermal analyzer (Seiko Instruments, TG/DTA6300). The specific surface area and pore size distribution were obtained from N$_2$ adsorption-desorption isotherms (Bel Japan, Inc., BELSORP-max).

Electrochemical characterizations of uc-TiO$_2$(B)/MWCNT Composite Materials: 2032-type coin cells were assembled using TiO$_2$(B)/MWCNT (cathode, Φ = 1.4 cm) and lithium metal (anode, Φ = 1.5 cm) electrodes. Cathodes were prepared by mixing the TiO$_2$(B)/MWCNT composite with polyvinylidene difluoride (PVdF) in a 90:10 mass ratio in n-methyl pyrrolidone (NMP). The mixture was then coated on a Cu foil (current collector) and dried at 80 °C under vacuum (ultimate vacuum = 0.67 Pa) for 12 h. The electrode was ≈20 µm thick with weight loading of 0.4 mg cm^{-2}. The electrolyte was a 1.0 M solution of lithium tetrafluoroborate (LiBF$_4$) dissolved in a

mixture of ethylene carbonate (EC): dimethyl carbonate (DMC) (50:50 in volume ratio). 25 µm thick polypropylene film (Celgard2400) was used as separator. Charge–discharge tests were performed between 1.0–3.0 V versus Li/Li$^+$ under constant current mode at various current densities ranging from 1 to 300 C rate assuming a 1 C-rate = 335 mA g^{-1}. Three-electrode characterization was made by using cavity microelectrode (CME) technique.[32] The CME consists of a thin platinum wire (Φ = 60 µm) with a cavity of 30 µm Φ and 40 µm deep sealed in a glass.

Supporting Information

Supporting Information is available from the Wiley Online Library or from the author.

Acknowledgements

[1] J. Miller, P. Simon, *Science* **2008**, *321*, 651.
[2] L. L. Zhang, X. S. Zhao, *Chem. Soc. Rev.* **2009**, *38*, 2520.
[3] K. Naoi, S. Ishimoto, J. Miyamoto, W. Naoi, *Energy Environ. Sci.* **2012**, *5*, 9363.
[4] K. Naoi, W. Naoi, S. Aoyagi, J. Miyamoto, T. Kamino, *Acc. Chem. Res.* **2013**, *46*, 1075.
[5] V. Augustyn, P. Simon, B. Dunn, *Energy Environ. Sci.* **2014**, *7*, 1597.
[6] E. Lim, C. Jo, H. Kim, M.-H. Kim, Y. Mun, J. Chun, J. Ye, J. Hwang, K.-S. Ha, K. Roh, K. Kang, J. Lee, *ACS Nano* **2015**, *9*, 7497.
[7] Z. Chen, V. Augustyn, J. Wen, Y. Zhang, M. Shen, B. Dunn, Y. Lu, *Adv. Mater.* **2011**, *23*, 791.
[8] V. Augustyn, J. Come, M. A. Lowe, J. W. Kim, P.-L. Taberna, S. H. Tolbert, H. D. Abruña, P. Simon, B. Dunn, *Nat. Mater.* **2013**, *12*, 518.
[9] J. Li, Z. Tang, Z. Zhang, *Chem. Mater.* **2005**, *17*, 5848.
[10] N. Taniguchi, M. Kato, K. Hirota, *J. Jpn. Soc.* **2012**, *59*, 326.
[11] C. W. Mason, I. Yeo, K. Saravanan, P. Balaya, *RSC Adv.* **2013**, *3*, 2935.
[12] M. Wei, Z.-M. Qi, M. Ichihara, I. Honma, H. Zhou, *Chem. Phys. Lett.* **2006**, *424*, 316.
[13] G. Armstrong, A. R. Armstrong, J. Canales, P. G. Bruce, *Electrochem. Solid State Lett.* **2006**, *9*, A139.
[14] J. Li, W. Wan, H. Zhou, J. Li, D. Xu, *Chem. Commun.* **2011**, *47*, 3439.
[15] Y. Furuya, W. Zhao, M. Unno, H. Noguchi, *Electrochim. Acta.* **2014**, *136*, 266.
[16] T. Shen, X. Zhou, H. Cao, C. Zheng, Z. Liu, *RSC Adv.* **2015**, *5*, 22449.
[17] C. Chen, X. Hu, Z. Wang, X. Xiaoqin, P. Hu, Y. Hang, *Carbon* **2014**, *69*, 302.
[18] H. Liu, Z. Bi, X.-G. Sun, R.-R Unocic, M.-P. Paranthaman, S. Dai, G.-M Brown, *Adv. Mater.* **2011**, *23*, 3450.
[19] H. Huang, Z. Yu, W. Zhu, Y. Gan, Y. Xia, X. Tao, W. Zhang, *J. Phys. Chem. Solids* **2014**, *75*, 619.
[20] S. Liu, H. Jia, L. Han, J. Wang, P. Gao, D. Xu, J. Yang, S. Che, *Adv. Mater.* **2012**, *24*, 3201.
[21] Y. Ren, Z. Liu, F. Pourpoint, A.-R. Armstrong, C.-P. Grey, P.-G. Bruce, *Angew. Chem.* **2012**, *124*, 2206.

[22] Q. Wang, Z. Wen, J. Li, *Adv. Funct. Mater.* **2006**, *16*, 2141.

[23] S. Liu, Z. Wang, C. Yu, H.-B. Wu, G. Wang, Q. Dong, J. Qiu, A. Eychmüller, X.-W. Lou, *Adv. Mater.* **2013**, *25*, 3462.

[24] V. Etacheri, J.-E. Yourey, B.-M Bartlett, *ACS Nano* **2014**, *8*, 1491.

[25] Y. Zhhang, Q. Fu, Q. Xu, X. yan, R. Zhang, Z. Guo, F. Du, Y. Wei, D. Zhang, G. Chen, *Nanoscale* **2015**, *7*, 12215.

[26] X. Yan, Y. Li, M. Li, Y. Jin, F. Du, G. Chen, Y. Wei, *J. Mater. Chem. A* **2015**, *3*, 4180.

[27] M. Kakihara, M. Kobayashi, K. Tomita, V. Petrykin, *Bull. Chem. Soc. Jpn* **2010**, *83*, 1285.

[28] M. Fehse, M. B. Yahia, L. Monconduit, F. Lemoigno, M.-L. Doublet, F. Fischer, C. Tessier, L. Stievano, *J. Phys. Chem. C* **2014**, *118*, 27210.

[29] A. G. Dylla, G. Henkelman, K. J. Stevenson, *Acc. Chem. Res.* **2013**, *46*, 1104.

[30] Y. Ishi, K. Okumura, T. Matsushita, S. Kawasaki, *Mater. Express* **2012**, *2*, 23.

[31] C. Arrouvel, S. C. Parker, M. S. Islam, *Chem. Mater.* **2009**, *21*, 4778.

[32] J. Come, P. L. Taberna, S. Hamelet, C. Masquelier, P. Simon, *J. Electrochem. Soc.* **2011**, *158*, A1090.

[33] J. Wang, J. Polleux, J. Lim, B. Dunn, *J. Phys. Chem. C* **2007**, *111*, 14925.

[34] A. Byeon, M. boota, M. Beidaghi, K. V. Aken, J. W. lee, Y. Gogotsi, *Electrochem. Commun.* **2015**, *60*, 199.

[35] K. Naoi, S. Ishimoto, N. Ogihara, Y. Nakagawa, S. Hatta, *J. Electrochem. Soc.* **2009**, *156*, A52.

[36] K. Naoi, S. Ishimoto, Y. Isobe, S. Aoyagi, *J. Power Sources* **2010**, *195*, 6520.